remote sensing

Article

Time-Series Analysis of Mining-Induced Subsidence in the Arid Region of Mongolia Based on SBAS-InSAR

Yuxin Xie [1], Hasi Bagan [1,†], Luwen Tan [1], Terigelehu Te [1], Amarsaikhan Damdinsuren [2] and Qinxue Wang [3,*,†]

[1] School of Environmental and Geographical Sciences, Shanghai Normal University, Shanghai 200234, China; hasibagan@staff.shnu.edu.cn (H.B.); 1000529963@smail.shnu.edu.cn (T.T.)
[2] Institute of Geography and Geoecology, Mongolian Academy of Sciences, Ulaanbaatar 13330, Mongolia
[3] Regional Environment Conservation Division, National Institute for Environmental Studies, Tsukuba 305-8506, Japan
* Correspondence: wangqx@nies.go.jp
† These authors contributed equally to this work.

Abstract: Mongolia's substantial mineral resources have played a pivotal role in its economic progress, with mining activities significantly contributing to this development. However, these continuous mining operations, particularly at the Oyu Tolgoi copper and gold mine, have induced land subsidence that threatens both production activities and poses risks of geological and other natural disasters. This study employs the Small Baseline Subset Interferometric Synthetic Aperture Radar (SBAS-InSAR) technique to monitor and analyze time-series surface subsidence using 120 Sentinel-1A datasets from 2018 to 2022. The findings reveal that the SBAS-InSAR method successfully captures the subsidence and its spatial distribution at Oyu Tolgoi, with the maximum cumulative subsidence reaching −742.01 mm and the highest annual average subsidence rate at −158.11 mm/year. Key drivers identified for the subsidence include variations in groundwater levels, active mining operations, and changes in surface stress. This research underscores the ongoing subsidence issue at the Oyu Tolgoi mining area, providing crucial insights that could aid in enhancing mining safety and environmental conservation in the region.

Keywords: surface subsidence; SBAS-InSAR; Oyu Tolgoi; long-term monitoring; Sentinel-1A

check for updates

Citation: Xie, Y.; Bagan, H.; Tan, L.; Te, T.; Damdinsuren, A.; Wang, Q. Time-Series Analysis of Mining-Induced Subsidence in the Arid Region of Mongolia Based on SBAS-InSAR. *Remote Sens.* **2024**, *16*, 2166. https://doi.org/10.3390/rs16122166

Academic Editors: Michalis Diakakis, Emmanouil Psomiadis, Georgios Deligiannakis and Aggelos Pallikarakis

Received: 30 April 2024
Revised: 3 June 2024
Accepted: 12 June 2024
Published: 14 June 2024

1. Introduction

The Mongolian economy is highly reliant on mineral extraction, focusing particularly on gold, copper, and coal, with over 250 active mining operations reported as of 2022 [1,2]. While the mining sector has propelled economic growth through job creation, foreign investment, and increased household incomes [3], it has also led to severe ecological issues. These include environmental degradation, water and air pollution, soil erosion, desertification, and, notably, surface subsidence, which are collectively contributing to significant geo-hazards [4–11].

Remote sensing, including traditional and advanced Interferometric Synthetic Aperture Radar (InSAR) technologies, has been pivotal in monitoring these impacts. Traditional methods such as GPS and leveling, despite their precision, are limited by high costs and labor intensity and lack the capability for extensive area coverage [12]. In contrast, InSAR technologies, including Differential Interference Radar (DInSAR), Small Baseline Subset InSAR (SBAS-InSAR), and Persistent Scatterer InSAR (PS-InSAR), offer expansive and high-resolution monitoring capabilities, proving essential in arid and mining regions [13–19].

Oyu Tolgoi (OT), one of the world's largest copper and gold mines, is located in Mongolia's Gobi region, which is currently facing severe droughts and water shortages exacerbated by mining activities. These conditions not only lead to vegetation loss and increased sandstorms but also pose a risk of land subsidence, threatening local ecosystems and the safety of the area's inhabitants [20–22].

Given the lack of extensive research on the Oyu Tolgoi mine's subsidence issues, this study employs the SBAS-InSAR technique to monitor and analyze the spatiotemporal evolution of surface subsidence from 2018 to 2022 using Sentinel-1A data. This research aims to elucidate the causes of subsidence at the OT mine and provide data critical for ensuring the mine's operational safety and environmental protection.

2. Materials

2.1. Study Area

The Oyu Tolgoi (OT) mining area, situated in the Khanbogd soum of Mongolia's South Gobi province, is one of the world's premier sites for copper and gold extraction. Positioned within the expansive Gobi Desert, the mine lies approximately 560 km south of Ulaanbaatar, the capital of Mongolia, and about 80 km north of the Chinese border. Its geographical coordinates span from 42°58′30″N to 43°03′00″N latitude and from 106°47′30″E to 106°55′00″E longitude (Figure 1).

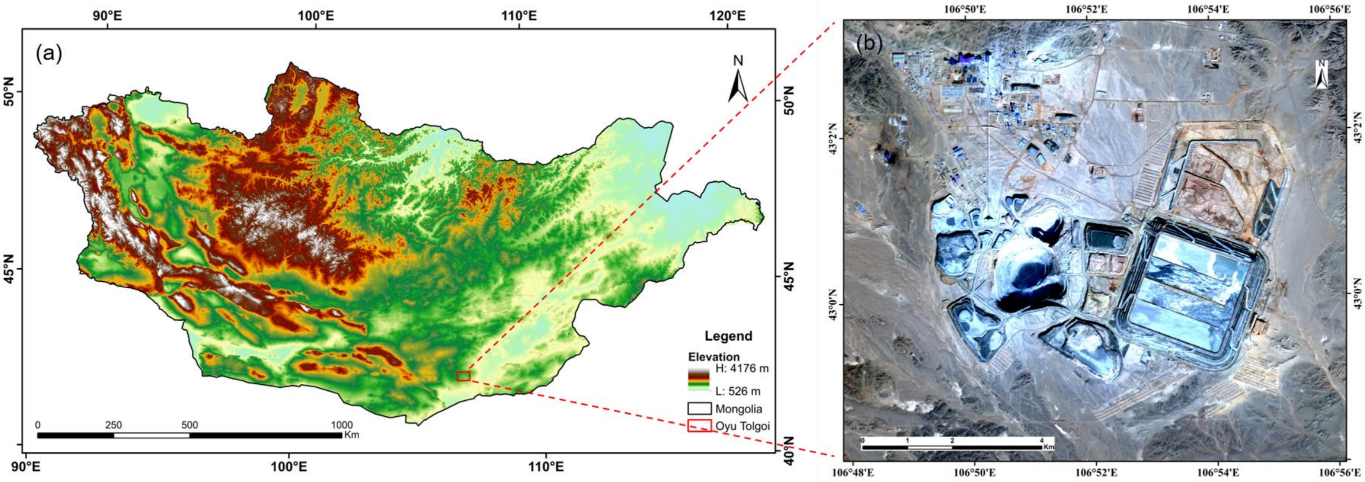

Figure 1. Geographical location of the study area—(**a**) Digital elevation model (DEM) of Mongolia; (**b**) Sentinel-2 image of OT mine on 30 December 2022.

Since Mongolia transitioned to a market economy in 1990, OT has emerged as a cornerstone for the nation's economic development, showcasing its significant mineral wealth. The mining operations are concentrated within a mineralized corridor that extends about 8 km in length and 1 km in width, oriented north–northeast. This corridor encompasses several mining zones, with the main zones centered in the area. These zones vary in elevation from approximately 1140 m above sea level (masl) to 1215 masl, divided into four primary mineralized areas: southwest, south, central, and far north. The predominant extractions from this mine are copper and gold, which are critical to Mongolia's mining output.

2.2. Datasets

The surface deformation in the Oyu Tolgoi (OT) mining area has been meticulously monitored using the Sentinel-1A SAR datasets, a key component of the European Space Agency's (ESA) Copernicus Earth Observation Programme. Equipped with a C-band Synthetic Aperture Radar (SAR), Sentinel-1A boasts a revisit period of 12 days, enabling it to provide consistent, all-weather, day-and-night observations globally.

For this study, data were captured in Interferometric Wide Swath (IW) mode with VV polarization. This mode was chosen due to its suitability for capturing wide-area surface deformations with high resolution. Based on the vector files of the study area, Sentinel-1A datasets were collected from the Alaska Satellite Facility (ASF) (https://search.asf.alaska.edu/, accessed on 12 February 2023), selecting 120 coherent single-look complex (SLC) scenes from Path 84, Frame 135 recorded during an ascending orbit, covering the entire year from 2018 to 2022. The images offer a pixel spacing of 2.3 m in slant range and 13.9 m in azimuth, detailed further in Table 1.

Table 1. Summary of Sentinel-1A images used in this study.

Sentinel-1A Data Parameters					
No.	**Acq. Date**	**No.**	**Acq. Date**	**No.**	**Acq. Date**
1	11 January 2018	41	30 May 2019	81	7 January 2021
2	23 January 2018	42	11 June 2019	82	19 January 2021
3	4 February 2018	43	23 June 2019	83	31 January 2021
4	28 February 2018	44	5 July 2019	84	12 February 2021
5	12 March 2018	45	17 July 2019	85	24 February 2021
6	24 March 2018	46	29 July 2019	86	8 March 2021
7	5 April 2018	47	10 August 2019	87	20 March 2021
8	17 April 2018	48	22 August 2019	88	1 April 2021
9	29 April 2018	49	3 September 2019	89	13 April 2021
10	11 May 2018	50	15 September 2019	90	25 April 2021
11	23 May 2018	51	27 September 2019	91	7 May 2021
12	4 June 2018	52	21 October 2019	92	19 May 2021
13	16 June 2018	53	2 November 2019	93	6 July 2021
14	28 June 2018	54	14 November 2019	94	11 August 2021
15	10 July 2018	55	26 November 2019	95	23 August 2021
16	22 July 2018	56	8 December 2019	96	4 September 2021
17	3 August 2018	57	20 December 2019	97	16 September 2021
18	15 August 2018	58	13 January 2020	98	28 September 2021
19	27 August 2018	59	6 February 2020	99	10 October 2021
20	8 September 2018	60	18 February 2020	100	22 October 2021
21	20 September 2018	61	1 March 2020	101	3 November 2021
22	2 October 2018	62	13 March 2020	102	15 November 2021
23	14 October 2018	63	25 March 2020	103	27 November 2021
24	26 October 2018	64	6 April 2020	104	9 December 2021
25	7 November 2018	65	18 April 2020	105	14 January 2022
26	19 November 2018	66	30 April 2020	106	26 January 2022
27	1 December 2018	67	12 May 2020	107	7 February 2022
28	13 December 2018	68	24 May 2020	108	19 February 2022
29	25 December 2018	69	5 June 2020	109	3 March 2022
30	18 January 2019	70	17 June 2020	110	15 March 2022
31	30 January 2019	71	29 June 2020	111	27 March 2022
32	11 February 2019	72	11 July 2020	112	8 April 2022
33	23 February 2019	73	23 July 2020	113	20 April 2022
34	7 March 2019	74	4 August 2020	114	2 May 2022
35	19 March 2019	75	16 August 2020	115	26 May 2022
36	31 March 2019	76	21 September 2020	116	25 July 2022
37	12 April 2019	77	3 October 2020	117	6 August 2022
38	24 April 2019	78	15 October 2020	118	22 November 2022
39	6 May 2019	79	20 November 2020	119	4 December 2022
40	18 May 2019	80	2 December 2020	120	28 December 2022

'No.' is the scene number of the 120 scenes and 'Acq. Date' is the acquisition date of Sentinel-1A.

Crucial to the SBAS-InSAR process is the use of precise orbit files, which ensure exact alignment between the SAR images over time, enhancing the inversion accuracy and yielding more precise deformation results [23]. Accordingly, precise orbit determination ephemeris data (https://scihub.copernicus.eu/gnss/#/home, accessed on 13 February 2023) corresponding to the Sentinel-1A images were employed. Additionally, the Shuttle Radar Topography Mission (SRTM) Digital Elevation Model (DEM) from NASA (http://gdex.cr.usgs.gov/gdex/, accessed on 16 February 2023), with a spatial resolution of 30 m, was utilized for orbit refining and topographic flattening.

3. Methods

This study harnesses Synthetic Aperture Radar (SAR) technology combined with Small Baseline Subset (SBAS) interferometric processing to analyze spatiotemporal deformation patterns in the Oyu Tolgoi mining area, situated in Mongolia's Gobi Desert. Sentinel-1A orbit lifting data were utilized, with the reliability of the inversion results cross-validated using Persistent Scatterer InSAR (PS-InSAR) technology and prior studies on groundwater levels.

3.1. InSAR, DInSAR, and Time-Series InSAR

InSAR is a three-dimensional surface morphology information extraction technique that uses the phase information of SAR images for interferometric processing, thus enabling the extraction of surface elevation information [24]. DInSAR technology is an extension of InSAR technology. It mainly uses the phase information from SAR satellite images to measure surface deformation [25–27]. DInSAR has gained significant prominence as a widely utilized technique for deformation monitoring.

However, DInSAR processing is subject to various errors. Although deformation censuses can be performed, the limited accuracy of deformation does not allow for a detailed depiction of deformation over time-series and, thus, has certain shortcomings in the monitoring and warning of deformation. Several researchers have proposed different types of time-series InSAR analysis techniques to address the limitations of DInSAR [28–31]. Over two decades of progress and data accumulation have led to the gradual shift from traditional DInSAR to time-series InSAR as the primary method for acquiring surface deformation data. This approach can be categorized into two main types: PS-InSAR primarily for urban built-up areas and SBAS-InSAR mainly for countryside vegetation areas [32].

3.2. Principles of SBAS-InSAR

The SBAS-InSAR technology proposed by Berardino is a time-series InSAR method that can be used to monitor the temporal evolution of surface deformations [33]. Although it can be simply understood as a combination of multiple DInSAR, SBAS-InSAR effectively minimizes spatial and temporal correlation and atmospheric disturbances, enhancing measurement accuracy and enabling time-series analysis. Compared to labor-intensive traditional geodetic surveys like leveling and GPS, which struggle with large-area surface deformation monitoring, SBAS-InSAR offers efficient, all-weather, and wide-coverage deformation monitoring [34].

It obtains a series of short spatial baseline interferometric pairs by setting specific temporal and spatial baseline thresholds. Then, it performs differential interferometric processing on these interferometric pairs and utilize high-pass filtering of the temporal thresholds and low-pass filtering of the spatial thresholds to remove atmospheric interferences, so as to obtain the correct unwrapped phase information. Finally, the singular value decomposition (SVD) method was employed to invert the time-series deformation results based on the flexible combination of interferograms within a subset. The basic principles are as follows.

Assuming that there are $N+1$ SAR images covering the same area acquired in a time-series $(t_0, \ldots, t_N)$ and selecting one of them as the master image, the remaining images are aligned to it. Then, interferometric pairs are combined to produce M differential interferograms based on the spatiotemporal baseline threshold, where

$$\frac{(N+1)}{2} \le M \le N\left(\frac{N+1}{2}\right) \tag{1}$$

Taking the moment t_0 as the reference moment, $\varphi(t_i)$ is the differential phase at the time $t_i(i = 1, \ldots, N)$. For the I-th differential interferogram generated at t_A and t_B, the interference phase value of any pixel (r, x) is

$$\delta\varphi_i(r,x) = \varphi(t_A, r, x) - \varphi(t_B, r, x) \approx \delta\varphi_{def,i} + \delta\varphi_{top,i} + \delta\varphi_{atm,i} + \delta\varphi_{noi,i} \tag{2}$$

where $\delta\varphi_{def,i}$ is the line-of-sight (LOS) deformation phase; $\delta\varphi_{top,i}$ is the terrain phase error; $\delta\varphi_{atm,i}$ is the atmospheric phase error; and $\delta\varphi_{noi,i}$ is the noise phase error. Eliminating the terrain phase, atmosphere, and noise, the expression of $\delta\varphi_i(r, x)$ can be simplified as

$$\delta\varphi_i(r,x) \approx \delta\varphi_{def,i} = \frac{4\pi}{\lambda}[d(t_A, r, x) - d(t_B, r, x)] \tag{3}$$

where λ is the is the wavelength of the radar signal, and $d(t_A, r, x)$ and $d(t_B, r, x)$ are the LOS cumulative deformations at moments t_A and t_B, respectively. To derive a physically meaningful subsidence sequence, Equation (3) is formulated as the product of the average phase velocity and the time interval between two acquisition times:

$$v_i = \frac{\varphi_i - \varphi_{i-1}}{t_i - t_{i-1}} \tag{4}$$

The value of the *i*-th differential interferogram can be reformulated as

$$\delta\varphi_i = \sum\nolimits_{k=t_{A,i+1}}^{t_{B,i}} (t_k - t_{k-1})v_k \tag{5}$$

In other words, it represents the integration of the velocity over each time period across the master and slave image time intervals. Equation (5) can be rewritten into the matrix form as

$$Bv = \delta\varphi \tag{6}$$

Equation (6) is a matrix with the dimension of M × N. If there are more than one small baseline sets, matrix B exhibits a rank deficiency. In such situations, the SVD method can be employed to perform the singular value decomposition of coefficient matrix B, allowing for the joint solution of multiple small baseline sets. Consequently, a least-squares solution was obtained, minimizing the norm of the cumulative shape variable and resulting in the estimation of the shape variable.

3.3. Data Processing

The processing of surface deformation data acquired through the SBAS-InSAR technique is comprehensive, encompassing several key phases: data preprocessing, SBAS-InSAR processing, and result visualization. Initially, the 120 collected SAR images were imported, aligned with precise orbit files, and clipped to precisely fit the study area. After that, SBAS-InSAR processing was performed. Finally, the results can be visualized. The primary steps of SBAS-InSAR processing include the following:

(1) Connection Graph Generation: This step involves estimating the baseline and selecting the primary image for the dataset. The image taken on March 10 was designated as the super master image, and all other images were processed in a multi-view setup.

(2) Interference Processing: This stage processes all interferometric pairs to generate coherence, perform flattening, filter data, and unwrap phases, resulting in unwrapped interferograms. External Digital Elevation Model (DEM) data were utilized here to simulate and correct the topographic phase, enhancing the accuracy of the results.

(3) Orbit Refining and Re-flattening: Involves selecting control points to refine the orbit and correct the flattened data. The software automatically selects several Ground Control Points (GCPs) to estimate the residual phase in the initial unwrapping phase and remove any residual topographic phase.

(4) SBAS Inversion: Comprises two distinct inversions. The first inversion estimates deformation rates and residual topography. The second inversion processes these estimates further to optimize the deformation results, refining the output for better accuracy. In this step, the SVD method was utilized to invert the time-series deformation results and the time-series surface subsidence maps were generated in the SAR coordinate system.

(5) Geocoding: This final step sets a specific threshold to ensure the reliability of time-series deformation results. These results are then geocoded and converted from the SAR coordinate system to the geographic coordinate system, making them suitable for practical use and analysis.

Figure 2 illustrates the SBAS-InSAR technique, showing these five primary steps in detail, which effectively capture the complex process of transforming raw SAR data into actionable geospatial information.

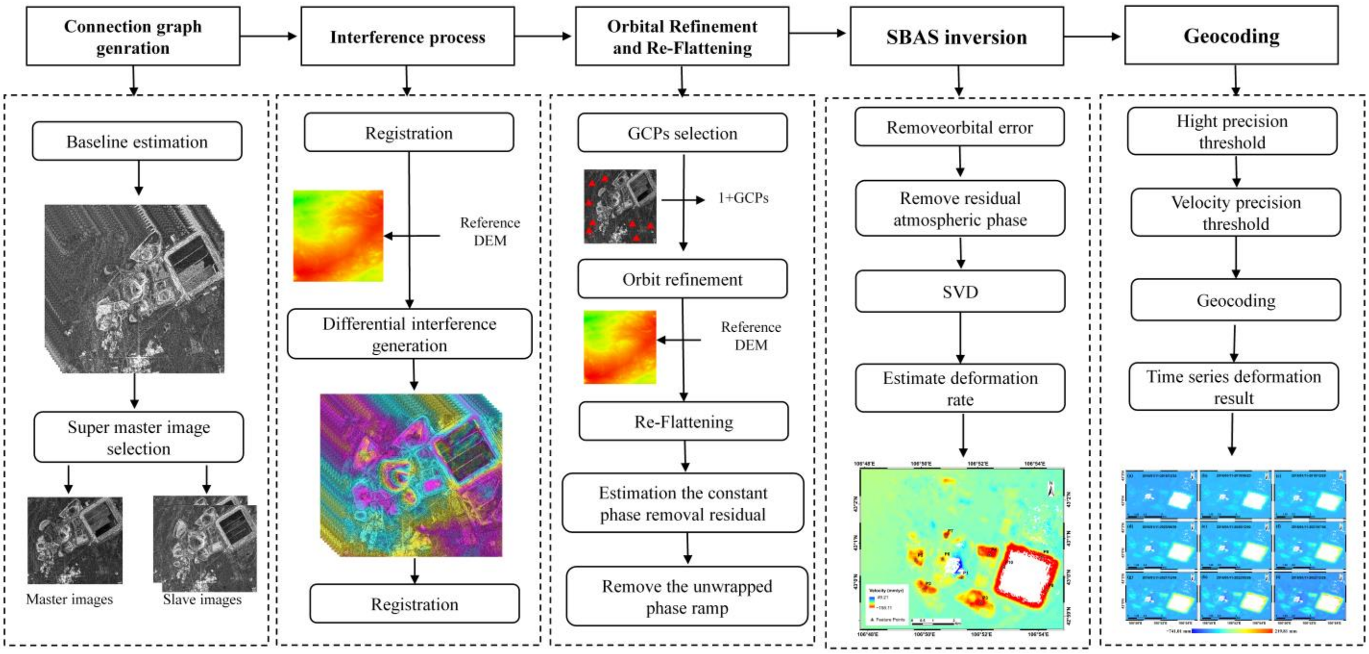

Figure 2. Workflow of SBAS-InSAR technique.

4. Results

4.1. Characteristics of surface subsidence

As determined in Section 2.2, the SAR image from 10 March 2020, was used as the super master image. Figure 3 presents the spatiotemporal baseline diagram, which includes both the Time Baseline Map and the Spatial Baseline Map. In this figure, yellow dots represent the super master images, green dots denote the other SAR images, and the line segments between them depict the interferometric pairs used.

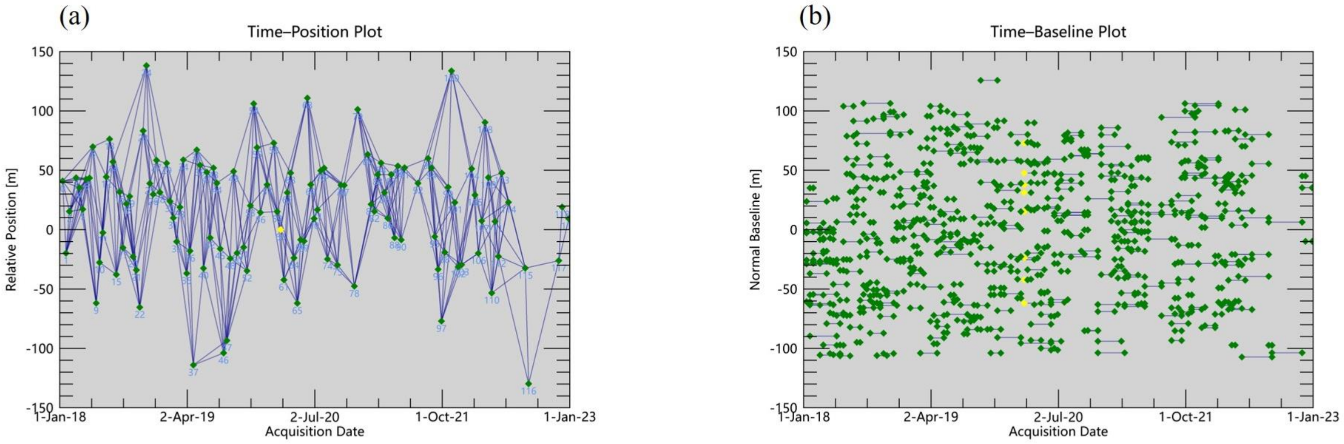

Figure 3. Spatiotemporal baseline diagram—(**a**) Time Baseline Map; (**b**) Spatial Baseline Map.

The interferometric processing of these pairs involved the use of the Goldstein filtering method and the Minimum Cost Flow (MCF) technique for untangling, which helped generate clear differential interferograms while eliminating topographic phase influences. Out of the 471 filtered interferograms, three were selected for their significant depiction of surface deformation. Figure 4 shows these interferograms with clear interference fringes, indicating deformation within the mining area.

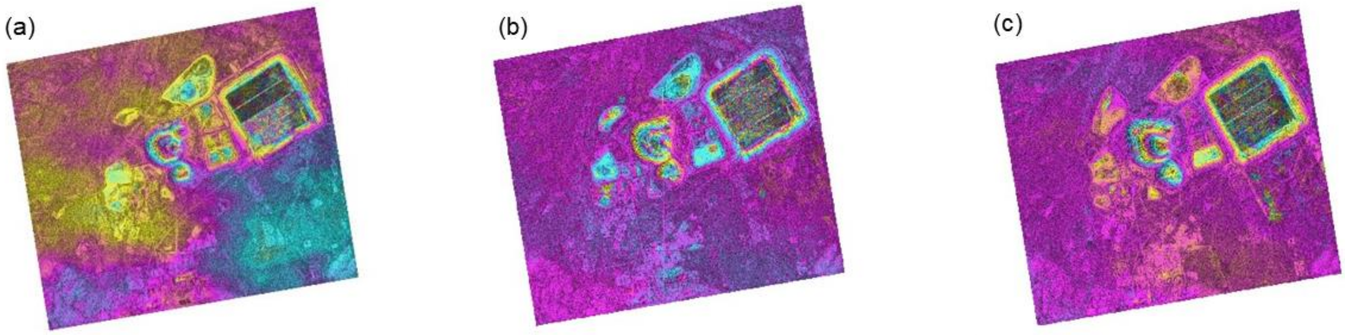

Figure 4. Filtered differential interferograms—(**a**) Filtered differential interferogram generated from two images acquired on 19 April 2018 and 3 May 2018; (**b**) Filtered differential interferogram generated from two images acquired on 8 March 2020 and 2 January 2020; (**c**) Filtered differential interferogram generated from two images acquired on 14 January 2022 and 7 February 2022.

After completing the SBAS inversion and geocoding steps, the final surface deformation data for the OT mining area were obtained and graphically represented. Figure 5 displays the annual average surface deformation rates, highlighting areas of subsidence and uplift.

The satellite line-of-sight (LOS) velocity map (Figure 5) illustrates that red and yellow areas, which indicate negative deformation rates, signify subsidence—i.e., the ground surface moving away from the satellite. Conversely, blue areas show positive deformation rates, indicating uplift—i.e., the ground surface moving towards the satellite. Most of the OT mine area is shown in yellow and red, with a few areas showing blue. This means the OT mine workings predominantly underwent significant subsidence with notably high rates, while a minor section of the region exhibited slight uplift during this time. The varying shades of red highlight different degrees of subsidence, with darker reds indicating more severe subsidence, which means that the subsidence velocity varied among the different areas. Moreover, the subsidence velocity decreases gradually from the center outwards. Notably, the darkest red square area on the right exhibits the highest subsidence velocity, with parts of the areas experiencing an annual average subsidence velocity of

−158.11 mm/year. Such a high rate of subsidence annually may have serious implications for infrastructure stability, mining safety, and the environment. Additionally, a slight uplift is noted in a blue-colored area within the mine. Outside the primary working zones, the terrain of the OT mine remains relatively stable with no significant changes in elevation.

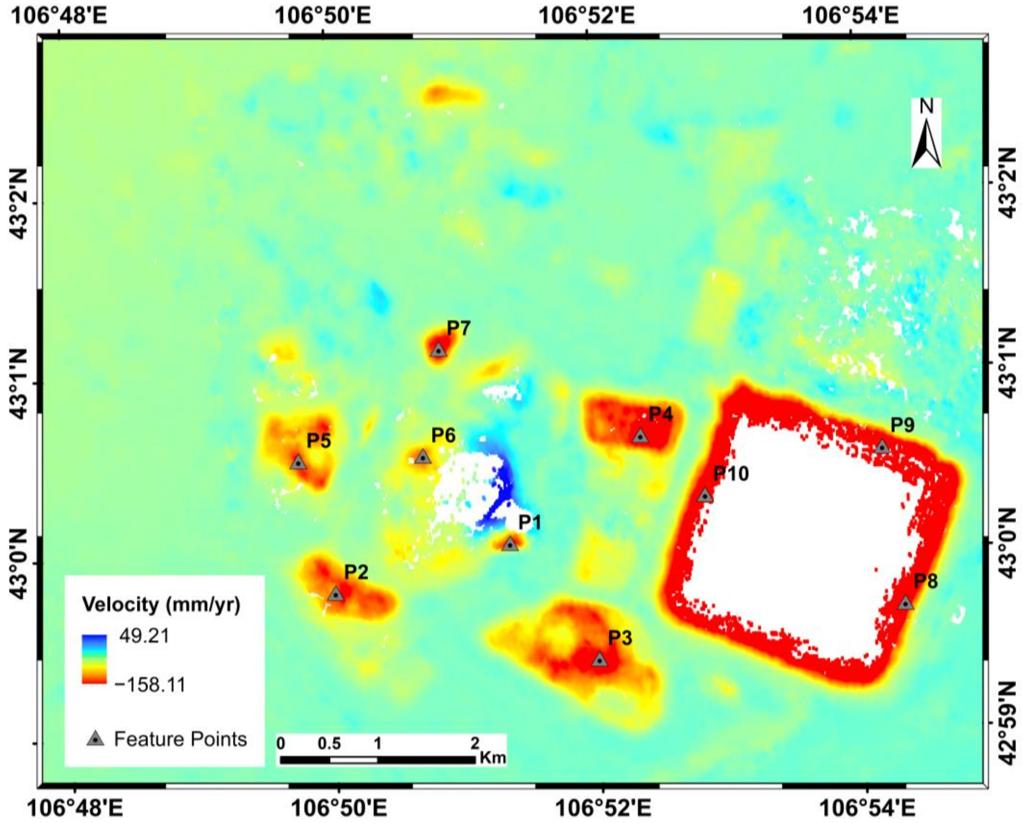

Figure 5. Annual average surface deformation rate (unit: mm/year) with P1 to P10. P1 to P10 indicate ten characteristic subsidence points used for comprehensive time-series subsidence analysis in Section 4.2.

4.2. Time-Series Analysis of Surface Subsidence

To analyze the temporal variability of surface subsidence at the OT mine site over this period, we mapped and compared accumulated surface deformation data from 11 January 2018, to 28 December 2022 (Figure 6). This figure highlights nine cumulative surface deformation datasets across various time intervals, offering a nuanced view of the temporal and spatial dynamics within the OT mining regions. Over the study period, specific areas of the mine exhibited a progressive increase in uplift, denoted by an intensifying blue hue. In contrast, conspicuous yellow and red discolorations emerged, signaling the gradual development of subsidence funnels.

These findings indicate ongoing surface subsidence from 2018 to 2022, with the affected area and the degree of subsidence both expanding over time. Notably, the central area showed higher cumulative subsidence compared to the peripheral edges. The water storage areas on the mine's right side recorded the highest cumulative subsidence, with parts of the areas experiencing a cumulative subsidence of −741.01 mm from 2018 to 2022.

Figure 5 presents the meticulous selection of ten characteristic subsidence points within the primary subsidence zones, chosen for comprehensive subsidence analysis. The distribution of these points varies within the study area. Specifically, P1 to P7 are situated near the mining area, while P8 to P10 are positioned in the water storage area, all integral to the primary operational zones. Simultaneously, these points exhibit varying degrees of subsidence. To investigate the temporal evolution of subsidence at specific feature points, a time-series subsidence map was generated for each one. Figure 7 illustrates that P2 and P6 display minor subsidence, followed by P1, P3, P5, and P7. P4, P8, and P10 exhibit more substantial subsidence, with P9 demonstrating the most significant subsidence, with the overall cumulative subsidence in the range [0, −400] mm over time. Furthermore, we note that the variation in cumulative subsidence at each point remains relatively minimal until 2020. However, starting from that point, these differences progressively intensify.

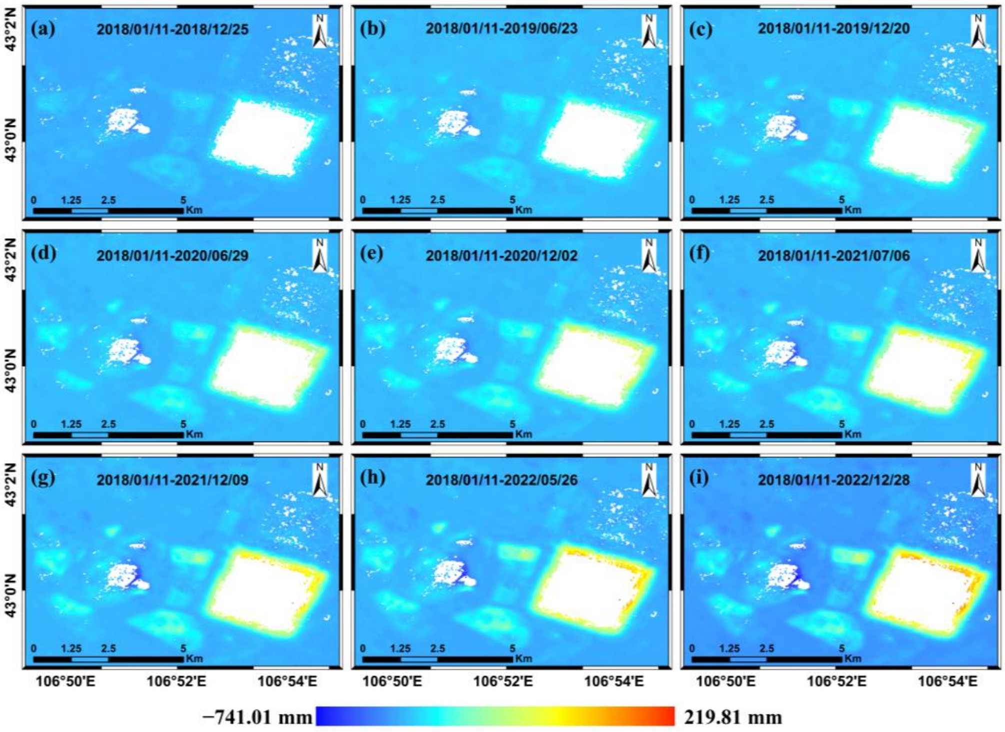

Figure 6. Spatiotemporal distribution of accumulated surface deformation in the study area.

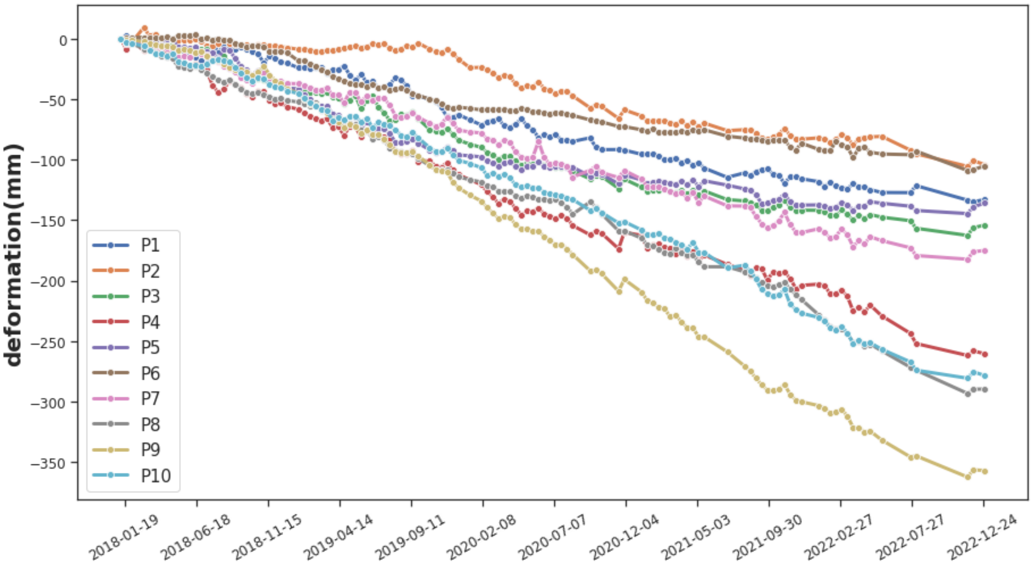

Figure 7. Time-series subsidence map of feature points.

4.3. Deformation Velocity Analysis

To facilitate the analysis of deformation rates, the data were categorized and visually represented through a color grading system. This stratification helps in understanding the varying velocities of surface deformation and its spatial distribution patterns across different regions of the OT mine. As depicted in Figure 8, the mine area has been segmented into zones labeled A through F, reflecting different subsidence characteristics.

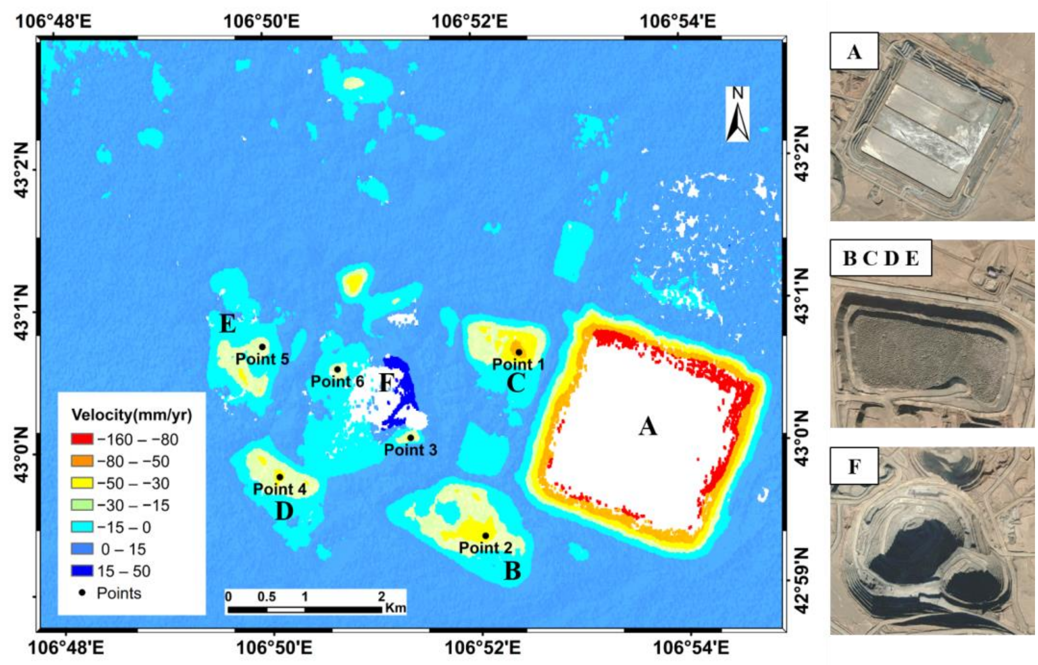

Figure 8. Annual average surface deformation classified rate. Maps to the right are from Google Earth for December 2018. The Points 1 to 6 are six example points used for correlation analysis in Section 5.

In this figure, subsidence is indicated by a spectrum from red to light blue, with red representing the most severe subsidence rates. Uplift is shown in shades of blue, with darker blues indicating higher uplift rates. To aid detailed analysis, subsidence rates were categorized into five classes:

- Class I: [−160, −80] mm/year;
- Class II: [−80, −50] mm/year;
- Class III: [−50, −30] mm/year;
- Class IV: [−30, −15] mm/year;
- Class V: [−15, 0] mm/year.

Zone A shows the most pronounced subsidence, with concentric color bands progressing from red at the center to light blue at the outer edges, representing a decrease in subsidence severity from Class I through Class V. Zones B, C, D, and E display similar patterns, with subsidence decreasing from the center outward. Specifically, Zone C transitions from orange at the center through yellow, green, and light blue, corresponding to Class II through Class V subsidence rates, respectively. Zones B, D, and E exhibit gradients from yellow to light blue, indicating Classes III to V.

Notably, Zone F illustrates a unique pattern with subsidence shown in yellow on the left side, while uplift is depicted by dark blue on the right. Blank areas in the map indicate regions where monitoring data are unavailable.

4.4. Precision Analysis of SBAS-InSAR Surface Deformation Results

Conducting field-level surveys for data validation at the OT site and obtaining usable GNSS data is extremely challenging due to stringent policies and regulations as well as lack of instrumentation deployment such as GNSS. In the absence of direct empirical data, cross-validation methods such as PS-InSAR are frequently utilized to confirm the reliability of monitoring outcomes [35,36]. Correlation analysis was conducted on the deformation using both SBAS-InSAR and PS-InSAR techniques, which showed great correlation, as depicted in Figure 9. In addition, numerous studies have consistently indicated a strong link between surface subsidence and groundwater levels [37,38]. Specifically, in the OT mine area, Okadera et al. [39] noted significant reductions in groundwater depths, ranging from 0.11 to 1.64 m, thereby highlighting the substantial environmental impacts resulting from mining activities.

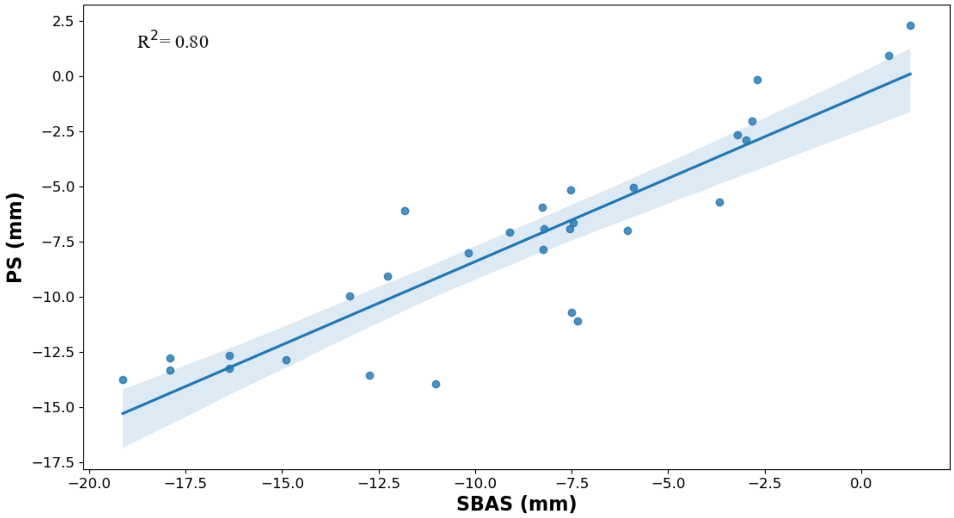

Figure 9. Accuracy verification.

5. Discussion

This section explores the potential factors influencing surface subsidence at the OT mine site, focusing on changes in surface stress, mining activities, and groundwater levels. As shown in Figure 8, the mine area has been categorized into six distinct zones (A to F), each exhibiting unique subsidence characteristics based on their geological and operational contexts.

Zone A, which includes the mine's water storage and adjacent wetland areas, experiences more pronounced subsidence compared to other regions. This is likely due to the accumulation of silt, suspended sediments, and organic matter that consolidate over time, resulting in substantial ground settlement [40]. Zones B through E, characterized by the presence of mineral sands, experience consolidation settlement as loose soils are compacted and dehydrated under external pressures. These areas are inherently prone to subsidence due to the geological processes involved [41]. Zone F, marked by its open-pit mining operations, displays varied subsidence patterns: substantial subsidence in the western and southern sectors, and slight elevation in the north, possibly from the accumulation of slag from ongoing mining activities. The above factors may contribute to the spatial variations of subsidence.

Tables 2 and 3 detail the mineral extraction data from the OT mine's annual reports [42,43] and surface cumulative subsidence records between 2018 and 2022, respectively. Notably, except for Point 5, subsidence at the mine has progressively increased alongside the volume of extracted minerals (Table 2). Figure 10a illustrates a strong positive correlation between cumulative subsidence and mining activities at selected sites, with correlation coefficients all surpassing 0.89 ($p < 0.05$), suggesting that ongoing mining activities significantly contribute to the observed surface subsidence.

Table 2. Annual mineral mined.

Year	2018	2019	2020	2021	2022
Mineral Mined (Million tons)	91	101	98	85	97
Cumulative Mineral Mined (Million tons)	91	192	290	375	473

Table 3. Cumulative subsidence of six example points (see Figure 8 for location).

Year	2018	2019	2020	2021	2022
Point 1	61.02	132.61	192.87	245.06	299.24
Point 2	49.76	105.44	147.36	181.81	203.41
Point 3	24.13	71.65	103.79	127.75	147.97
Point 4	14.58	46.70	112.67	143.71	149.14
Point 5	23.47	85.88	107.60	122.97	119.72
Point 6	11.27	53.12	69.79	93.26	109.05

unit: mm

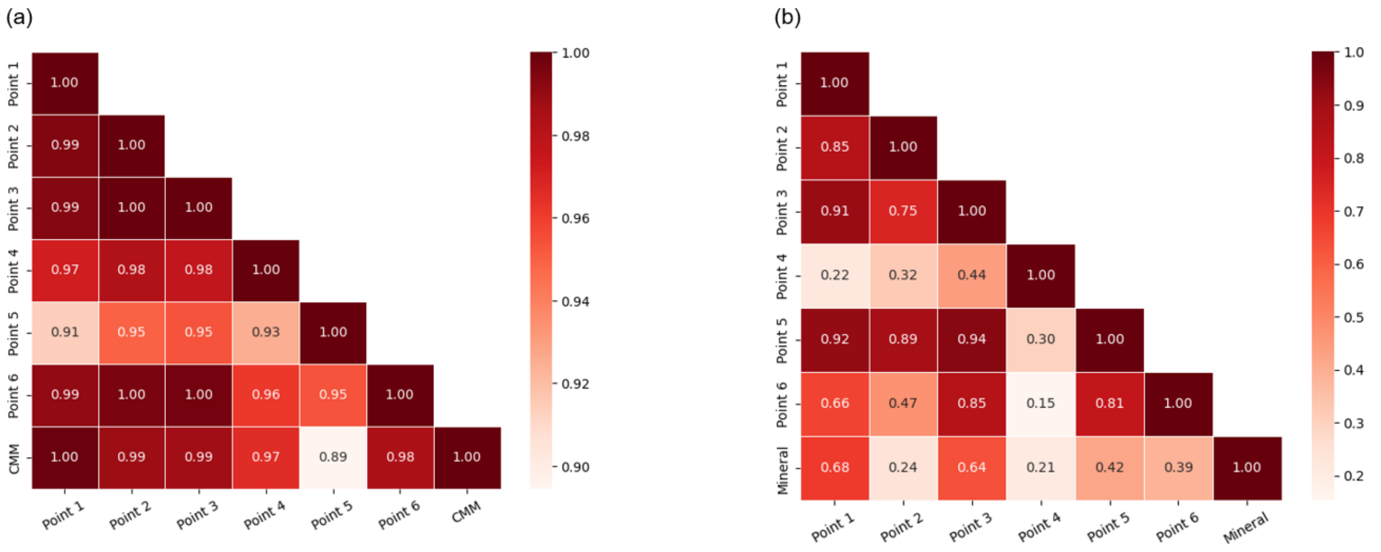

Figure 10. Correlation matrix—(**a**) Correlation matrix of cumulative subsidence and cumulative mineral mined (CMM refers to cumulative mineral mined); (**b**) Correlation matrix of annual subsidence and annual minerals mined ('Mineral' refers to mineral mined).

Furthermore, Figure 10b examines the correlation between annual subsidence levels and mineral extraction across different mining areas. Points 1, 3, 5, and 6, which are closer to active mining zones, show higher correlation with annual mining outputs compared to Points 2 and 4. This differential suggests that proximity to mining activities plays a crucial role in the extent of surface deformation experienced, as mining operations likely alter surface stress and induce rock mass deformations, such as collapses and fractures [44,45].

The impact of groundwater extraction on surface subsidence at the mine site was further explored. The OT mine, located in the arid South Gobi region of Mongolia, where water resources are scarce, heavily relies on groundwater to meet its operational needs due to the insufficiency of surface water. Figure 11 depicts the significant volumes of groundwater extracted annually from 2016 to 2020 [46], which have led to alterations in groundwater levels, potentially triggering terrain subsidence above the extraction sites.

Subsequent well monitoring near the mine site has shown a notable decrease in water levels, with reductions ranging from 16 to 46 m below established benchmarks across 28 wells, as reported by the Human Pipeline Groundwater Palace. These findings are consistent with observations by Okadera et al. [39], who noted declines in groundwater levels from 0.11 to 1.64 m in the OT mine area, and Nakayama et al. [47], who documented significant decreases in the Galba River's groundwater levels due to mining activities starting in 2010. These consistent studies and reports indicate the decline in groundwater levels is also a contributing factor to surface subsidence at the mine site, as it causes subsurface rocks to expand and contract [48].

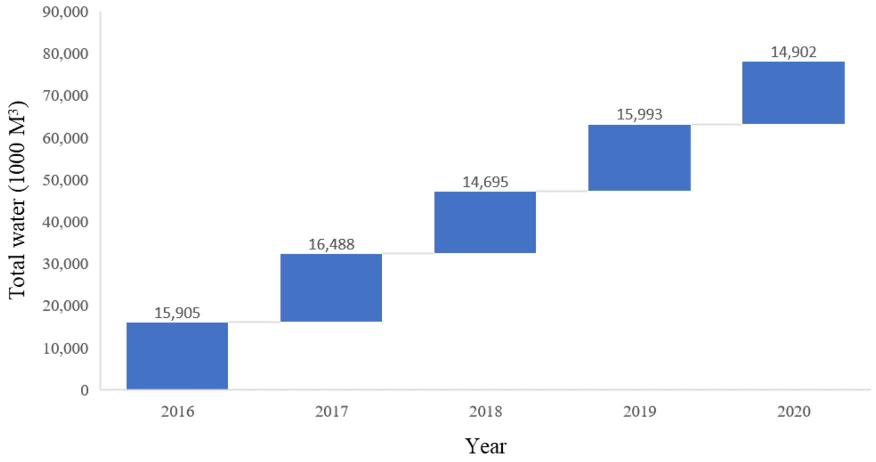

Figure 11. Total water withdrawn from wells from 2016 to 2020 (unit: 1000 M^3).

SBAS-InSAR-based measurements have been instrumental in providing essential insights for the sustainable development of mining sites. However, despite these advances, challenges persist, including unmeasured deformation at specific mining locations and extensive blank areas within the study zone. These issues may arise from data decoherence during differential interference, a limitation of InSAR noted by Ferretti et al. [49], or from rapid and extensive changes over brief intervals. Consequently, data decoherence obscures part of the measured region, leading to their appearance as blanks on the deformation result map. Notably, the blank regions in Zones A and F are primarily due to significant daily water level fluctuations and variations in the vertical heights of stockpiles, which induce decoherence and complicate the monitoring process.

This study leveraged SBAS-InSAR technology to explore surface subsidence at the OT mine site, yet several limitations are notable:

(1) Spatial Coverage: SBAS-InSAR's reliability depends on the coherence of satellite images over time. Rapid landscape changes due to mining or natural processes can disrupt this coherence, limiting the accuracy of subsidence measurements.
(2) Temporal Resolution: the 12-day revisit cycle of the Sentinel-1A satellite may miss rapid subsidence events, potentially leading to underestimations of subsidence rates and extents.
(3) Vertical Accuracy: despite corrections for atmospheric effects, inherent limitations due to atmospheric disturbances and the satellite's viewing angle may still impact the vertical accuracy of measurements.
(4) Supplementary Data: The study's validation and analysis of subsidence is limited by the availability and accuracy of measured data, GNSS data, groundwater data, and mining volumes. Correlating subsidence with groundwater levels is also challenged by the sporadic availability and variable accuracy of groundwater data, complicating the establishment of a direct causative relationship.
(5) External Factors and Generalizability: the analysis does not extensively cover other potential subsidence drivers, like geological processes or external human activities, and findings may not apply to other regions with different conditions.

Future research should address these limitations by integrating more frequent imaging, refined groundwater data, refined mining volumes, measured data, available GNSS data, and broader environmental factors to enhance the robustness and applicability of the findings. To mitigate the potential threats of subsidence to infrastructure stability, mining safety, water resources, and the environment, it is necessary for OT mines to adopt the following measures to reduce ongoing subsidence: continuous on-site monitoring, reinforcement of infrastructure, improved management of water resources, and a reduction in groundwater extraction [50–52].

6. Conclusions

This study leveraged Sentinel-1A data from 2018 to 2022 and SBAS-InSAR technology to effectively monitor and analyze surface subsidence at the OT mine in Mongolia. It successfully delineated the spatiotemporal characteristics of subsidence and pinpointed key contributing factors. The significant findings are as follows:

Substantial Subsidence: the OT mine has experienced notable surface subsidence, with the most severe cumulative decrease reaching -742.01 mm and the highest annual subsidence rate at -158.11 mm/year.

Efficacy of SBAS-InSAR: This technology has proven extremely effective in arid, sparsely vegetated areas like the OT mine, showcasing its enhanced capability for accurate subsidence detection and making it a valuable tool for monitoring similar environments.

Influential Factors: the analysis confirmed that significant fluctuations in groundwater levels, changes in surface stress, and intensive mining activities are the primary drivers behind the observed subsidence.

These insights are valuable both practically and academically; they inform sustainable mining practices and contribute to geological hazard prevention worldwide, while also enriching the understanding of subsidence monitoring in Mongolian mining regions and similar settings.

Despite its contributions, this study acknowledges limitations related to the temporal and spatial resolution of SBAS-InSAR technology, which may overlook rapid subsidence events and experience data coherence issues in dynamic environments. Additionally, the variability in groundwater data accuracy and the challenges in generalizing findings underscore the need for caution.

Future research should focus on mitigating subsidence in mining areas by integrating a broader spectrum of environmental data, including high-frequency InSAR images and detailed groundwater measurements. Such an approach promises a more comprehensive evaluation of long-term impacts and the refinement of monitoring technologies applicable to diverse geological settings. By addressing the current limitations, further studies can improve prediction accuracy and broaden the scope of these findings to more global applications.

Author Contributions: Conceptualization, Y.X.; Methodology, L.T.; Data processing, L.T.; Validation, Y.X.; Investigation, Y.X.; Data curation, A.D.; Writing—original draft, Y.X.; Writing—review & editing, Q.W.; Visualization, T.T.; Supervision, A.D. and Q.W.; Project administration, H.B.; Funding acquisition, H.B. and Q.W. All authors have read and agreed to the published version of the manuscript.

Funding: This work was supported by National Key R&D Program of China (No. 2022YFE0119500) and the Research on Advancement of Climate Change Impact Assessment Methodology (No. 2125AA130).

Data Availability Statement: The data presented in this study are available on request from the corresponding author. The data are not publicly available due to privacy.

Acknowledgments: The authors wish to express their gratitude to the colleagues and staff at the School of Environmental and Geographical Sciences, Shanghai Normal University for their support and invaluable contributions throughout the course of this research. We are also grateful for the funding support received from the National Key R&D Program of China (No. 2022YFE0119500) and the Research on Advancement of Climate Change Impact Assessment Methodology (No. 2125AA130), National Institute for Environmental Studies of Japan, which made this research possible. Lastly, our gratitude extends to all the peer reviewers and editors for their constructive comments that significantly improved the manuscript.

Conflicts of Interest: The funders had no role in the design of the study; in the collection, analyses, or interpretation of data; in the writing of the manuscript; or in the decision to publish the results.

References

1. Schoderer, M.; Karthe, D.; Dombrowsky, I.; Dell'Angelo, J. Hydro-social dynamics of miningscapes: Obstacles to implementing water protection legislation in Mongolia. *J. Environ. Manag.* **2021**, *292*, 112767. [CrossRef] [PubMed]
2. Zandariya, B. Improving the policy framework for financial assurance for mine closure in Mongolia. *Resour. Policy* **2022**, *77*, 102628. [CrossRef]
3. Batdelger, T.; Zagdbazar, M. Does mining improve rural livelihood?: Evidence from Mongolia. *Resour. Policy* **2022**, *78*, 102794. [CrossRef]
4. Fraser, J.; Kunz, N.C.; Batdorj, B. Can mineral exploration projects create and share value with communities? A case study from Mongolia. *Resour. Policy* **2019**, *63*, 101455. [CrossRef]
5. Prior, T.; Giurco, D.; Mudd, G.; Mason, L.; Behrisch, J. Resource depletion, peak minerals and the implications for sustainable resource management. *Glob. Environ. Chang.* **2012**, *22*, 577–587. [CrossRef]
6. Wantzen, K.M.; Mol, J.H. Soil erosion from agriculture and mining: A threat to tropical stream ecosystems. *Agriculture* **2013**, *3*, 660–683. [CrossRef]
7. Zhengfu, B.; Inyang, H.I.; Daniels, J.L.; Frank, O.T.T.O.; Struthers, S. Environmental issues from coal mining and their solutions. *Min. Sci. Technol.* **2010**, *20*, 215–223.
8. Zhang, L.; Zhai, Z.; Zhou, Y.; Liu, S.; Wang, L. The Landscape Pattern Evolution of Typical Open-Pit Coal Mines Based on Land Use in Inner Mongolia of China during 20 Years. *Sustainability* **2022**, *14*, 9590. [CrossRef]
9. Conde, M.; Le Billon, P. Why do some communities resist mining projects while others do not? *Extr. Ind. Soc.* **2017**, *4*, 681–697. [CrossRef]
10. Cui, X.; Wang, J.; Liu, Y. Prediction of progressive surface subsidence above longwall coal mining using a time function. *Int. J. Rock Mech. Min. Sci.* **2001**, *38*, 1057–1063. [CrossRef]
11. Ding, R.; Liu, H.; Yuan, G.; Dong, J. Deformation and subsidence prediction on surface of Yuzhou mined-out areas along middle route project of south-to-north water diversion, China. *Open Geosci.* **2018**, *10*, 834–843. [CrossRef]
12. Siriwardane, H.J.; Amanat, J. Analysis of subsidence caused by underground mining. *Int. J. Min. Sci. Technol.* **1984**, *2*, 271–290. [CrossRef]
13. Simons, M.; Fialko, Y.; Rivera, L. Coseismic deformation from the 1999 M w 7.1 Hector Mine, California, earthquake as inferred from InSAR and GPS observations. *Bull. Seismol. Soc. Am.* **2002**, *92*, 1390–1402. [CrossRef]
14. Nie, L.; Wang, H.; Xu, Y.; Li, Z. A new prediction model for mining subsidence deformation: The arc tangent function model. *Nat. Hazards* **2018**, *75*, 2185–2198. [CrossRef]
15. Wempen, J.M.; McCarter, M.K. Comparison of L-band and X-band differential interferometric synthetic aperture radar for mine subsidence monitoring in central Utah. *Int. J. Min. Sci. Technol.* **2017**, *27*, 159–163. [CrossRef]
16. Hui, X.; Ma, F.; Zhao, H.; Xu, J. Monitoring and statistical analysis of mine subsidence at three metal mines in China. *Bull. Seismol. Soc. Am.* **2019**, *78*, 3983–4001. [CrossRef]
17. Casu, F.; Manzo, M.; Lanari, R. A quantitative assessment of the SBAS algorithm performance for surface deformation retrieval from DInSAR data. *Remote Sens. Environ.* **2006**, *102*, 195–210. [CrossRef]
18. Kim, J.-R.; Lin, C.-W.; Lin, S.-Y. The use of InSAR phase coherence analyses for the monitoring of aeolian erosion. *Remote Sens.* **2021**, *13*, 2240. [CrossRef]
19. Ghorbani, Z.; Khosravi, A.; Maghsoudi, Y.; Mojtahedi, F.F.; Javadnia, E.; Nazari, A. Use of InSAR data for measuring land subsidence induced by groundwater withdrawal and climate change in Ardabil Plain, Iran. *Sci. Rep.* **2022**, *12*, 13998. [CrossRef] [PubMed]
20. Hongming, W.; Ruren, L.; Yiting, Q.; Zhuqing, L.I.; Jun, G. Application of time series InSAR technology in monitoring ground deformation of mining area: A case study at Huolinhe open pit mining area in Inner Mongolia. *Chin. J. Geol. Hazard Control* **2022**, *33*, 71–78. [CrossRef]
21. Zhou, D.; Wang, L.; An, S.; Wang, X.; An, Y. Integration of unmanned aerial vehicle (UAV)-based photogrammetry and InSAR for mining subsidence and parameters inversion: A case study of the Wangjiata Mine, China. *Bull. Seismol. Soc. Am.* **2022**, *81*, 343. [CrossRef]
22. Pawluszek-Filipiak, K.; Borkowski, A. Monitoring mining-induced subsidence by integrating differential radar interferometry and persistent scatterer techniques. *Eur. J. Remote Sens.* **2021**, *54*, 18–30. [CrossRef]
23. Yang, W.; He, Y.; Wang, W.H.; Chen, Y.D.; Chen, Y. InSAR monitoring of 3-D surface deformation in Jinchuan Mining area, Gansu Province. *Remote Sens. Nat. Resour.* **2022**, *34*, 177–188.
24. Wegmttller, U.; Strozzi, T.; Werner, C.; Wiesmann, A.; AG, G.R.S. Sar interferometry for topographic mapping and surface deformation monitoring. *FJP* **2002**, *18*, 24–32.
25. Massonnet, D.; Feigl, K.L. Radar interferometry and its application to changes in the Earth's surface. *Rev. Geophys.* **1998**, *36*, 441–500. [CrossRef]
26. Rosen, P.A.; Hensley, S.; Joughin, I.R.; Li, F.K.; Madsen, S.N.; Rodriguez, E.; Goldstein, R.M. Synthetic aperture radar interferometry. *Proc. IEEE* **2000**, *88*, 333–382. [CrossRef]
27. Hanssen, R.F. *Radar Interferometry: Data Interpretation and Error Analysis*; Kluwer Academic Publishers: Dordrecht, The Netherlands, 2001; pp. 1–307.

28. Ferretti, A.; Prati, C.; Rocca, F. Permanent scatterers in SAR interferometry. *IEEE Trans. Geosci. Remote Sens.* **2001**, *39*, 8–20. [CrossRef]
29. Colesanti, C.; Ferretti, A.; Novali, F.; Prati, C.; Rocca, F. SAR monitoring of progressive and seasonal ground deformation using the permanent scatterers technique. *IEEE Trans. Geosci. Remote Sens.* **2003**, *41*, 1685–1701. [CrossRef]
30. Hooper, A.; Zebker, H.A. Phase unwrapping in three dimensions with application to InSAR time series. *JOSA A* **2007**, *24*, 2737–2747. [CrossRef] [PubMed]
31. Rocca, F. Modeling interferogram stacks. *IEEE Trans. Geosci. Remote Sens.* **2007**, *45*, 3289–3299. [CrossRef]
32. Zhang, P.; Guo, Z.; Guo, S.; Xia, J. Land subsidence monitoring method in regions of variable radar reflection characteristics by integrating PS-InSAR and SBAS-InSAR techniques. *Remote Sens.* **2022**, *14*, 3265. [CrossRef]
33. Berardino, P.; Fornaro, G.; Lanari, R.; Sansosti, E. A new algorithm for surface deformation monitoring based on small baseline differential SAR interferograms. *IEEE Trans. Geosci. Remote Sens.* **2002**, *40*, 2375–2383. [CrossRef]
34. Li, S.; Xu, W.; Li, Z. Review of the SBAS InSAR Time-series algorithms, applications, and challenges. *Geod. Geodyn.* **2022**, *13*, 114–126. [CrossRef]
35. He, Y.; Yan, H.; Yang, W.; Yao, S.; Zhang, L.; Chen, Y.; Liu, T. Time-series analysis and prediction of surface deformation in the Jinchuan mining area, Gansu Province, by using InSAR and CNN–PhLSTM network. *IEEE J. Sel. Top. Appl. Earth Obs. Remote Sens.* **2022**, *15*, 6732–6751. [CrossRef]
36. Li, Z.; Wang, Z.; Liu, W.; Li, X.; Zhou, M.; Zhang, B. Detecting, Monitoring, and Analyzing the Surface Subsidence in the Yellow River Delta (China) Combined with CenterNet Network and SBAS-InSAR. *J. Spectrosc.* **2022**, *2022*, 2672876. [CrossRef]
37. Poland, J.; Davis, G. Subsidence of the land surface in the Tulare-Wasco (Delano) and Los Banos-Kettleman City area, San Joaquin Valley, California. *EOS Trans. Am. Geophys. Union* **1956**, *37*, 287–296. [CrossRef]
38. Motagh, M.; Shamshiri, R.; Haghighi, M.H.; Wetzel, H.U.; Akbari, B.; Nahavandchi, H.; Roessner, S.; Arabi, S. Quantifying groundwater exploitation induced subsidence in the Rafsanjan plain, southeastern Iran, using InSAR time-series and in situ measurements. *Eng. Geol.* **2017**, *218*, 134–151. [CrossRef]
39. Okadera, T.; Wang, Q.X.; Deni, E.; Nakayama, T. Groundwater monitoring for evaluating the pasture carrying capacity and its vulnerability in arid and semi-arid regions: A case study of urban and mining areas in Mongolia. *IOP Conf. Ser. Earth Environ. Sci.* **2019**, *266*, 012013. [CrossRef]
40. Shi, C.; Zhang, D.; You, L.; Li, B.; Zhang, Z.; Zhang, O. Land subsidence as a result of sediment consolidation in the Yellow River Delta. *J. Coast. Res.* **2007**, *23*, 173–181. [CrossRef]
41. Steckler, M.S.; Oryan, B.; Wilson, C.A.; Grall, C.; Nooner, S.L.; Mondal, D.R.; Akhter, S.H.; DeWolf, S.; Goodbred, S.L. Synthesis of the distribution of subsidence of the lower Ganges-Brahmaputra Delta, Bangladesh. *Earth-Sci. Rev.* **2022**, *224*, 103887. [CrossRef]
42. Oyu Tolgoi LLC. Year in Review 2020. 2021. Available online: https://www.ot.mn/media/otnew/content/reports/2020_YiR/20210428_Annual_report_2020-English.pdf (accessed on 7 March 2024).
43. Oyu Tolgoi LLC. Year in Review 2022. 2023. Available online: https://www.ot.mn/media/otnew/content/Year_in_review_2022.pdf (accessed on 7 March 2024).
44. Parsons, T.; Wu, P.C.; Wei, M.; D'Hondt, S. The weight of New York City: Possible contributions to subsidence from anthropogenic sources. *Earth's Future* **2023**, *11*, e2022EF003465. [CrossRef]
45. Kratzsch, H. *Mining Subsidence Engineering*; Springer: Berlin/Heidelberg, Germany, 1983; ISBN 978-3-642-81925-4.
46. Oyu Tolgoi LLC. *Audit Report on Water Use for the Bear Head Project 2016–2020*. 2022. Available online: https://www.ot.mn/media/otnew/content/Water_Audit_report_2021_Final_MNG.pdf (accessed on 7 March 2024).
47. Nakayama, T.; Wang, Q.; Okadera, T. Evaluation of spatio-temporal variations in water availability using a process-based eco-hydrology model in arid and semi-arid regions of Mongolia. *Ecol. Model.* **2021**, *440*, 109404. [CrossRef]
48. Donnelly, L.J. A review of international cases of fault reactivation during mining subsidence and fluid abstraction. *Q. J. Eng. Geol. Hydrogeol.* **2009**, *42*, 73–94. [CrossRef]
49. Ferretti, A.; Monti-Guarnieri, A.; Prati, C.; Rocca, F.; Massonet, D. *InSAR Principles: Guideline for SAR Interferometry Processing and Interpretation*; ESA Publication: Noordwijk, The Netherlands, 2007.
50. Sahu, P.; Lokhande, R.D. An Investigation of Sinkhole Subsidence and its Preventive Measures in Underground Coal Mining. *Procedia Earth Planet. Sci.* **2015**, *11*, 63–75. [CrossRef]
51. Kondolf, G.M.; Schmitt, R.J.P.; Carling, P.; Darby, S.; Arias, M.; Bizzi, S.; Castelletti, A.; Cochrane, T.A.; Gibson, S.; Kummu, M.; et al. Changing sediment budget of the Mekong: Cumulative threats and management strategies for a large river basin. *Sci. Total Environ.* **2018**, *625*, 114–134. [CrossRef] [PubMed]
52. Tang, W.; Zhao, X.; Motagh, M.; Bi, G.; Li, J.; Chen, M.; Chen, H.; Liao, M. Land Subsidence and Rebound in the Taiyuan Basin, Northern China, in the Context of Inter-Basin Water Transfer and Groundwater Management. *Remote Sens. Environ.* **2022**, *269*, 112792. [CrossRef]